J. Fluid Mech. (2016), *vol.* 808, *pp.* 539–561. © Cambridge University Press 2016
doi:10.1017/jfm.2016.635

Generation and stability of inertia–gravity waves

P. Maurer[1,†], **S. Joubaud**[1,†] **and P. Odier**[1,†]

[1]Univ Lyon, Ens de Lyon, Univ Claude Bernard Lyon 1, CNRS, Laboratoire de Physique, F-69342 Lyon, France

(Received 8 December 2015; revised 1 June 2016; accepted 27 September 2016; first published online 4 November 2016)

In the ocean, stratification and rotation allow for the existence of inertia–gravity waves. Instabilities of these waves, such as triadic resonant instability (TRI), may play a key role in the mixing process of the deep ocean. In an experimental set-up, we generate inertia–gravity waves which may become unstable depending on the background rotation and wave frequency. The instability produces secondary waves that match the spatial and temporal resonance conditions of TRI. The effect of rotation is introduced in a pre-existing theory and results in a prediction of the growth rate of TRI in the case of an infinite plane wave. The issue of finite size of the beam is then addressed using a simple model in which we show that the instability is enhanced in a given range of Coriolis parameter. Finally, we compare the experimental threshold of the instability with the model, and find good agreement except at higher rotation rate. At constant primary wave frequency, we analyse the evolution of the secondary wave characteristics with rotation. The appearance of unexpected sub-inertial secondary waves may be related to the discrepancy observed between predicted and experimental thresholds at higher rotation.

Key words: instability, internal waves, waves in rotating fluids

1. Introduction

In rotating stratified fluids, such as the oceans, waves called inertia–gravity waves can propagate. Their characteristics and their stability are driven by both the rotation, through the Coriolis parameter f, equal to twice the rotation rate Ω, and the stratification, through the buoyancy frequency $N = [(-g/\bar{\rho})(\mathrm{d}\rho/\mathrm{d}z)]^{1/2}$, where $\rho(z)$ is the density distribution ($\bar{\rho}$ is a reference value) over the vertical coordinate z and g is the acceleration of gravity. For the case in which the axes of rotation and gravity are antiparallel, the dispersion relation of the inertia–gravity waves is

$$\theta = \arcsin\left(\sqrt{\frac{\omega^2 - f^2}{N^2 - f^2}}\right), \tag{1.1}$$

where θ is the angle between the wave beam and the horizontal. Assuming $N > f$, the dispersion relation shows that propagating waves only exist for excitation frequencies

†Email addresses for correspondence: paco.maurer@ens-lyon.fr, sylvain.joubaud@ens-lyon.fr, philippe.odier@ens-lyon.fr

in the range $f < \omega < N$. One of the prominent processes that leads to transport of energy from large to small scales in the oceans is the parametric subharmonic instability (PSI). At laboratory scale, where viscosity is not negligible, this instability is referred to as triadic resonant instability (TRI) (see, e.g., Müller *et al.* (1986) and references therein). It is characterized by a primary internal wave giving birth to two secondary subharmonic waves through nonlinear triadic interaction (Benielli & Sommeria 1998; Koudella & Staquet 2006; Clark & Sutherland 2010; Gayen & Sarkar 2013). The instability occurs when temporal and spatial resonance are satisfied,

$$\omega_0 = \omega_1 + \omega_2, \tag{1.2}$$

$$\boldsymbol{k}_0 = \boldsymbol{k}_1 + \boldsymbol{k}_2, \tag{1.3}$$

where $\boldsymbol{k}$ is the wavevector and subscripts 0, 1 and 2 refer to the primary and two secondary waves respectively. As proved by Hasselmann (1967), this instability requires the frequencies (defined positive) of the secondary waves to be smaller than that of the primary wave. The difference interactions $\omega_1 - \omega_2 = \pm\omega_0$ are neutrally stable and therefore do not play a role in our study. In most cases, and specifically in oceanic conditions with larger Reynolds number, the secondary waves have a higher wavenumber, which makes them more prone to break and overturn, creating mixing (Staquet & Sommeria 2002).

In the non-rotating case, Bourget *et al.* (2013) showed good agreement between the theory for internal plane wave instability and experimental observations of the instability of a quasi-monochromatic internal wave beam. In the non-stratified case, similar experimental conclusions were reached by Bordes *et al.* (2012) in the case of purely inertial plane waves. Sutherland (2013) raised the question of the validity of these theories in the case of finite wave beams, which are more relevant for oceanic applications, where wave beams, emitted from the interaction of the barotropic tide and the sea-floor topography, can have a very narrow profile (Lien & Gregg 2001; Gostiaux & Dauxois 2007). The important role played by the finite size of the wave beam on TRI was investigated experimentally and a simple model was proposed in Bourget *et al.* (2014). A theoretical study was developed to understand how such wave beams differ, with regard to TRI, from monochromatic plane waves (Karimi & Akylas 2014). This theory confirms the experimental results of Bourget *et al.* (2014). Tackling the issue of a finite size beam in a rotating fluid experimentally might bring a new understanding on the transfer of energy between scales, on the secondary wave selection and on the open question of wave turbulence in the open ocean. To the best of our knowledge, there has been no experimental work in the laboratory on the importance of rotation on TRI. Such problems have been tackled numerically for a low-mode internal tide (Hazewinkel & Winters 2011) and theoretically for an inviscid scenario (Young, Tsand & Balmforth 2008). Both studies have shown that rotation is of paramount importance for the threshold and for the characteristics of TRI.

An important question in the oceanic context is the latitude dependence of TRI. Recent numerical and field studies have shown that when first-mode semidiurnal (M2) inertia–gravity tides travel from low latitude towards higher latitudes, they undergo a dramatic loss of energy near the latitude of 29° (MacKinnon 2005; MacKinnon *et al.* 2013*a*,*b*). This latitude, called the 'critical latitude', corresponds to a Coriolis frequency equal to half of the frequency of the primary wave. This loss might be linked to enhanced instability and a resultant large transfer of energy to the secondary waves (Hibiya 2004; Simmons 2008).

In this paper, we present an experimental study of the role of rotation on TRI as well as the influence of the beam width on this instability. In § 2, we present our

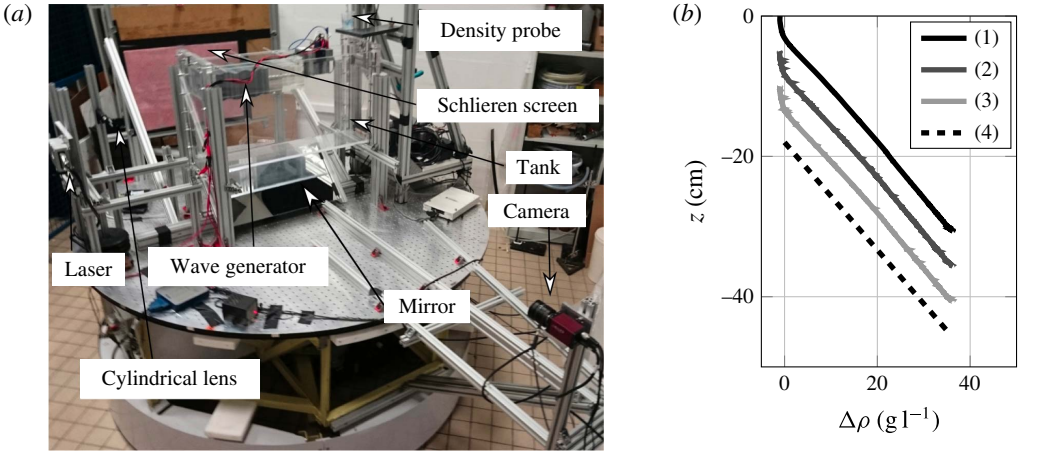

FIGURE 1. (Colour online) (*a*) Experimental set-up fixed to a rotating table, which permits the production of inertia–gravity waves in the tank, with controlled N and f. Synthetic schlieren and particle image velocimetry (PIV) are used to investigate the wave properties. (*b*) Density profile along the vertical axis z expressed as the difference between the measured density and the density of pure water. (1) Profile taken before rotation, (2) profile taken after linearly accelerating the table to 9.54 rpm during 15 min and (3) profile taken after 2 h of constant rotation at 9.54 rpm ($f = 2$ rad s^{-1}). It should be noted that this rotation rate, used here for the purpose of this test, is much larger than the values used for our experiments in what follows. The dashed line (4) is a linear adjustment leading to a value of $N = 1.13$ rad s^{-1}. For the sake of clarity, curves (2)–(4) are shifted vertically by respectively 5, 10 and 15 cm.

experimental set-up, study inertia–gravity wave generation and show that waves may be subject to TRI. The characteristics of the secondary waves are then compared in § 3 with theoretical values obtained from the inclusion of rotation in the theoretical framework derived in Bourget *et al.* (2013, 2014). Using this model, we infer the importance of finite size effects and apply it to the oceanic case. Finally, in § 4, we present measurements of the effect of rotation on the instability threshold and show that our theoretical analysis is in good agreement with the observations. We also focus in this section on how secondary wave characteristics are affected by rotation, and we interpret their evolution. We show the unexpected generation of waves below the Coriolis frequency. Some conclusions are drawn in the last section.

2. Experimental study

2.1. *Experimental set-up*

The experimental set-up, shown in figure 1(*a*), is similar to the one described in Bourget *et al.* (2013, 2014), with the exception that the whole apparatus is set in rotation on a turntable (PERPET, designed and constructed by GP Concept). The turntable is 1.92 m in diameter and its rotational velocity can be adjusted from $\Omega = 0$ to 60 rpm, which allows variations of the Coriolis parameter $f = 2\Omega$ from 0 to 12.5 rad s^{-1} with 0.1 % precision. The axis of rotation is aligned with gravity with 2 mm m^{-1}.

Experiments are conducted in a rectangular tank 80 cm long and 17 cm wide filled with linearly stratified fluid, i.e. a constant buoyancy frequency N, using the

standard double-bucket method (Fortuin 1960; Oster & Yamamoto 1963). Then, the experimental apparatus is set into rotation. In order to avoid mixing and to keep N unchanged, the angular acceleration is less than 10^{-3} rad s^{-2}. Figure 1(*b*) displays the density profile before rotation, after spin-up of the table and after two hours of constant rotation. On a time scale much larger than the typical experimental time (ca. 20 min), the variation of N is smaller than its accuracy, i.e. $\pm 0.25\,\%$. The linear fit of the profile gives the value of the buoyancy frequency, which is of the order of 1 rad s^{-1}. This is the typical value of N used in all of the experiments presented in this paper. We restricted our study to the case $f < N$. In this range of rotation rates, isopycnal deformation is very small (< 0.5 cm), which preserves the alignment of the background density gradient with gravity and with the rotation axis. For all of the experiments presented in this article, solid body rotation is established in the fluid.

The inertia–gravity waves are generated using a configuration identical to the one described in Bourget *et al.* (2013). The wave generator (Gostiaux *et al.* 2006; Mercier *et al.* 2010), consisting of stacked moving plates, is set horizontally at the surface in such a way that the plates move vertically. The time-dependent vertical motion of the generator is prescribed in the form

$$\zeta(x, t) = a(x)\cos(\omega_0 t - \ell_0 x), \tag{2.1}$$

where ω_0 is the frequency of the oscillations. This forcing sets the horizontal component of the wavevector, denoted ℓ_0, and no component in the transverse (y) direction. The amplitude $a(x)$ is constant (denoted a_0) over two wavelengths in the middle of the generator and is smoothly decreased over a half-wavelength on each side to avoid spurious inertia–gravity wave emission. In this paper, ℓ_0 and the amplitude are kept constant ($\ell_0 \approx 80$ m^{-1} and $a_0 = 5$ mm). The motion of the generator generates a plane wave of finite extent. The length of the tank is chosen to be long enough so that reflected waves are dissipated before coming back into the field of view.

As a preliminary step, particle image velocimetry (PIV) is performed in a horizontal plane 10 cm below the generator to observe the motion of the wave in the (x, y) plane and measure the transverse component of the velocity. The fluid is seeded with 2 mg l^{-1} of hollow glass particles (110 p8, sphericell). A horizontal laser sheet is created by a cylindrical lens, and observations are made via a mirror below the tank inclined at 45° (see figure 1*a*). The CIVx algorithm (Fincham & Delerce 2000) computes the cross-correlation between two successive images, giving the instantaneous horizontal two-dimensional velocity.

This velocity measurement in a horizontal plane shows that, as expected for linear inertia–gravity waves (Sutherland 2010), rotation induces a velocity component oriented in the transverse direction, v_y, proportional to the Coriolis parameter f. The main result of these measurements is, however, that no dependence in the y direction is observed: the wavevector is contained in the (x, z) plane, i.e. $\boldsymbol{k} \cdot \boldsymbol{e}_y = \boldsymbol{0}$. This result remains true in the bulk of the fluid, while in the first centimetre close to the wall a decrease of velocity is observed due to viscous boundary layers, previously observed for pure internal waves ($f = 0$) by Brouzet *et al.* (2016).

The absence of transverse gradients allows for the use of a synthetic schlieren technique (Sutherland *et al.* 1999; Dalziel, Hughes & Sutherland 2000), which is more accurate for the visualization and study of TRI (Bourget *et al.* 2014). The motion of the fluid is recorded in a vertical plane by a camera at 2 fps. The CIVx algorithm computes the cross-correlation between the real time and the $t = 0$ background image, when the fluid is at rest. The outcome is the instantaneous two-dimensional density-gradient field $\partial_x \rho'(x, z, t)$ and $\partial_z \rho'(x, z, t)$ where $\rho'(x, z, t) = \rho(x, z, t) - \rho_0(z)$, $\rho(x, z, t)$ and $\rho_0(z)$ being the instantaneous and initial fluid densities respectively.

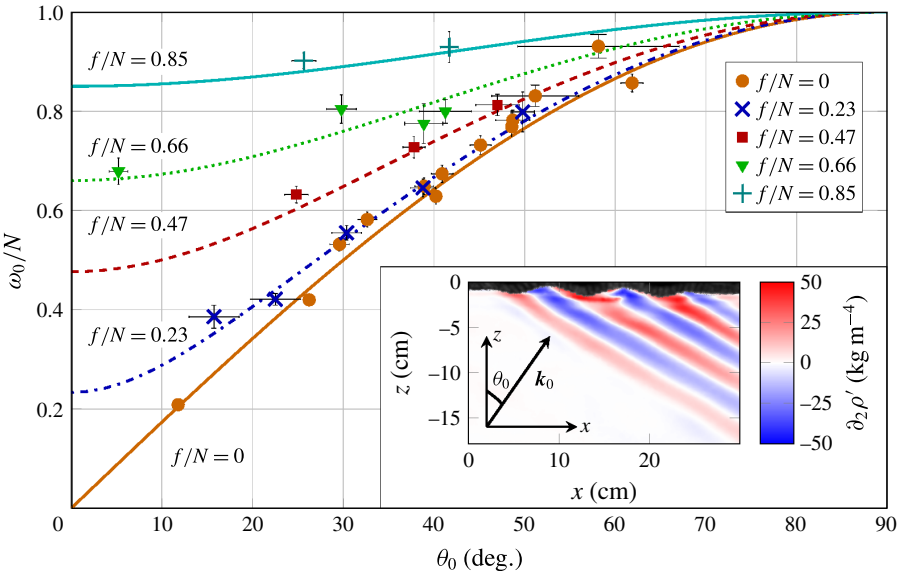

FIGURE 2. (Colour online) The dimensionless frequency ω_0/N of an inertia–gravity wave plotted versus the angle of propagation θ_0 defined in (2.2) for various values of the dimensionless Coriolis parameter f/N ranging from 0 to 0.85. The lines are theoretical predictions (from (2.2)) over which are plotted experimental measurements. For all of these experiments N was close to 1 rad s^{-1}. The inset shows a typical snapshot of a density-gradient field obtained from synthetic schlieren, for the following parameters: $\omega_0/N = 0.66$ and $f/N = 0.35$.

2.2. *Wave characteristics and dispersion relation*

A typical snapshot of a wave field produced by the generator and measured using synthetic schlieren is shown in the inset of figure 2. From such an image, the phase of the wave is extracted using the Hilbert transform method developed by Mercier, Garnier & Dauxois (2008) and previously used for pure internal waves (Bourget *et al.* 2013). From there, the components (ℓ_0, m_0) of the wavevector are obtained by linearly fitting the variation of the phase with x and z respectively. The error is estimated by the standard deviation of the difference between the measured values and the values predicted by the linear fit. In addition, from a single-point time series of the density-gradient field, the wave frequency, the peak of the spatial average of the fast Fourier transform of the time signal, can be extracted. Once these characteristics of the waves are obtained, one can check whether they satisfy the dispersion relation

$$\omega_0^2 = N^2 \sin^2\theta_0 + f^2 \cos^2\theta_0 = N^2 \frac{\ell_0^2}{\kappa_0^2} + f^2 \frac{m_0^2}{\kappa_0^2}, \tag{2.2}$$

where θ_0 is the angle of propagation such that $\boldsymbol{k}_0 = (\ell_0, 0, m_0) = \kappa_0(\sin\theta_0, 0, \cos\theta_0)$, where κ_0 is the magnitude of the wavevector $\boldsymbol{k}_0$. Figure 2 displays the wave frequency versus the angle of propagation θ_0, $\arctan(\ell_0/m_0)$, for several values of the Coriolis parameter. The result is consistent with the dispersion relation (2.2) for inertia–gravity waves, shown in the figure as lines. Even if our wavemaker was designed to generate pure internal waves, these two observations demonstrate that the wavemaker successfully generates well-defined inertia–gravity waves in the vertical plane (x, z) as long as f is smaller than $0.85N$. For larger values of f, we were unable to obtain

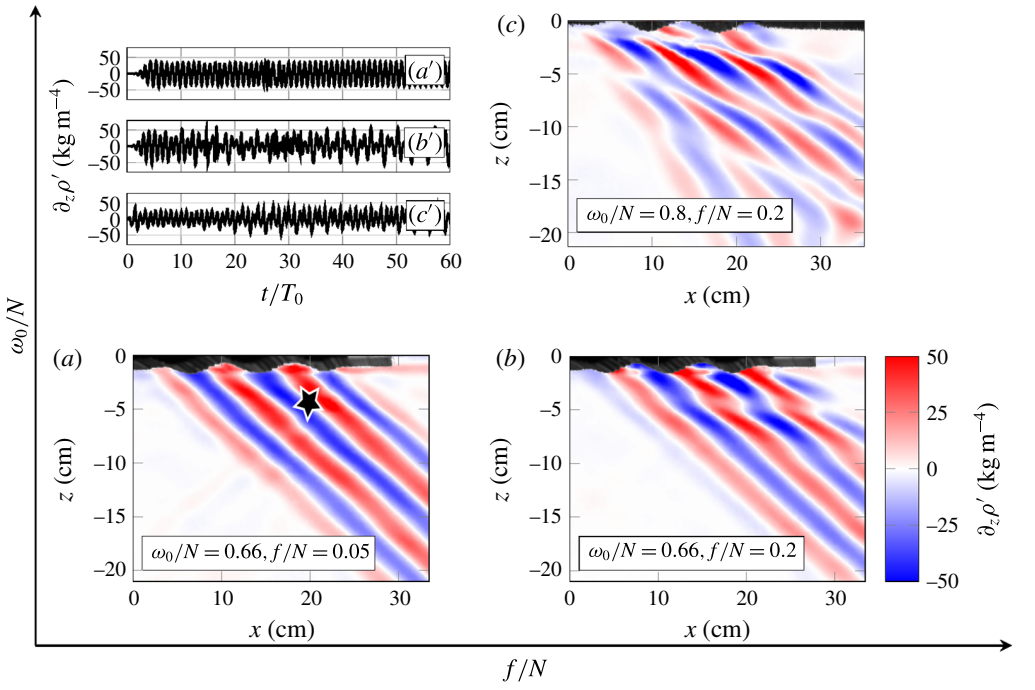

FIGURE 3. (Colour online) Snapshots of the vertical density field, $\partial_z\rho'(x, z, t)$, at $t = 50\ T_0$ displayed in an $(f/N, \omega_0/N)$ plane. The disposition of the snapshots indicates the relative importance of f/N and ω_0/N: (*a*) $(\omega_0/N, f/N) = (0.66, 0.05)$, (*b*) $(\omega_0/N, f/N) = (0.66, 0.2)$, (*c*) $(\omega_0/N, f/N) = (0.8, 0.2)$. For the three experiments, the wavemaker has the geometrical characteristics ($\ell_0 = 72$ m^{-1}, $a_0 = 5$ mm). The top left panels (a'), (b') and (c') show time series taken in respectively experiment (*a*), (*b*) and (*c*) at a point located 5 cm below the wavemaker, roughly at the centre of the wave beam (indicated by a star in wave field *a*).

a well-defined wave beam: the emitted wave had a much lower amplitude and a poorly defined wavelength. This problem may result from the lack of an imposed transverse velocity from the wavemaker. For $f/N \lesssim 1$, v_y becomes of the same order of magnitude as v_x, and there is a loss of efficiency of the wave generator in this range. In the study presented in this article, however, we did not need to consider cases with $f/N > 0.45$.

2.3. *An unstable plane wave*

Evolving in the (ω_0, f) parameter space, the observed wave field is not always as simple as shown in the inset of figure 2. Three examples of density-gradient fields, taken at different locations of the parameter space, are shown in figure 3. In the three cases, the amplitude a_0 and the horizontal component of the wavevector, ℓ_0, are the same. The corresponding time signals taken at a given location (indicated by a star in *a*) are also shown, in the top left corner. The signals are fairly stable after an initial transient of less than five periods, demonstrating that steady states are established for the frequencies and Coriolis parameter values considered.

For the lowest frequency and Coriolis parameter (case *a*), the wave field is described by straight lines for the density-gradient phase, and a single-point time signal oscillates sinusoidally. However, as f/N is increased (case *b*), there is a

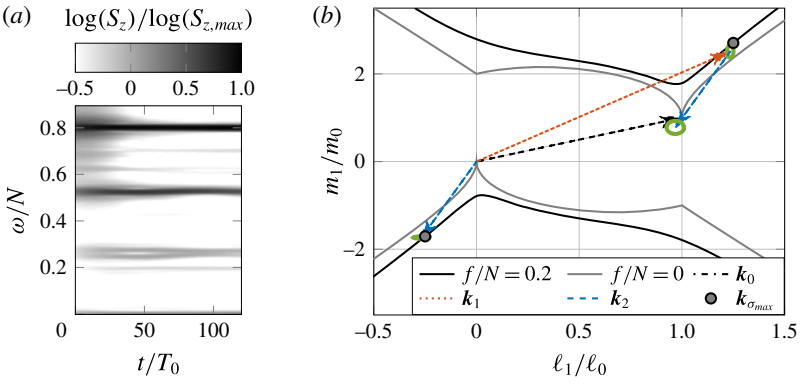

FIGURE 4. (Colour online) (*a*) The time–frequency diagram corresponding to the unstable wave presented in figure 3(*c*) ($\omega_0/N = 0.8$, $f/N = 0.2$, $\ell_0 = 72$ m^{-1}, $a_0 = 5$ mm). Here, S_z is the time–frequency spectrum of the vertical density-gradient field, computed on a $30T_0$ wide sliding time window. (*b*) The corresponding experimental measurement of secondary wave dimensionless wavevector components $\ell_{1,2}/\ell_0$ and $m_{1,2}/m_0$ of the same unstable wave. Ellipses represent the experimental errors as described in § 2.2. The black (grey) lines represent the theoretical resonance locus for $f/N = 0.2$ ($f/N = 0$). The positions corresponding to the maximum growth rate (3.6) are indicated by two grey circles.

modification of the wave field: in the first 5 cm there is a deformation of the phase lines, below which the primary wave amplitude is significantly decreased. This corresponds to the appearance of TRI. This feature is emphasized by the modulation of the time signal (panel *b*), which is typical of the appearance of new frequencies in the system. When ω_0/N is increased as well (case *c*), the TRI is fully developed. To obtain more information about TRI, the time–frequency response $S_z(\omega, t)$ of the corresponding signal (time series *c*) can be computed (Flandrin 1999):

$$S_z(\omega, t) = \left\langle \left| \int_{-\infty}^{+\infty} \mathrm{d}u\, \partial_z \rho'(u, x, z) \mathrm{e}^{\mathrm{i}\omega u} h(t-u) \right|^2 \right\rangle, \tag{2.3}$$

where h is a Hamming time window of chosen length. In figure 4(*a*), $S_z(\omega, t)$ indicates the appearance of two secondary waves growing in time, with frequencies ω_1 and ω_2 such that $\omega_1 + \omega_2 = \omega_0$.

The corresponding wavevectors, computed as in the previous subsection, are shown in figure 4(*b*) in an $(\ell/\ell_0, m/m_0)$ plane. They satisfy the spatial resonance condition $\boldsymbol{k}_0 = \boldsymbol{k}_1 + \boldsymbol{k}_2$. The corresponding theoretical resonance locus, obtained using the temporal and spatial resonance conditions and the dispersion relation for each of the three waves, is also shown. This curve depends naturally on the Coriolis parameter and is similar to the one presented by McComas & Bretherton (1977). In figure 4(*b*), we show this locus for two cases, $f/N = 0$ (no rotation) and $f/N = 0.2$. We observe that when f/N increases, the allowed range for the secondary vertical wavenumber increases whereas the allowed range for the secondary horizontal wavenumber shrinks, leading to secondary waves propagating more horizontally (recall that the wavevector is perpendicular to the group velocity). The tips of the vectors $\boldsymbol{k}_1$ and $\boldsymbol{k}_2$ are located, within experimental errors, on the curve that shows the theoretical resonance locus for the corresponding Coriolis parameter $f/N = 0.2$.

As a conclusion of this first set of observations, inertia–gravity waves can either be unstable through TRI or remain stable. Rotation seems to play a key role in this picture, by favouring the instability (at least in some cases like in figure 3) but also by changing the characteristics of the secondary waves. To gain insight into the role of rotation in TRI, we first present the theoretical framework for weak TRI of a viscous plane wave and then consider finite size effects on the wave beam.

3. Growth rate of TRI

3.1. *Infinite plane wave theoretical growth rate*

A general theory for TRI of an inviscid inertia–gravity wave beam was previously obtained by Young *et al.* (2008). Viscosity, however, is not negligible in laboratory experiments. The conditions under which TRI can develop have been theoretically presented for internal waves by Koudella & Staquet (2006) and Bourget *et al.* (2013) and for inertial waves by Bordes *et al.* (2012). This framework for weakly nonlinear infinite plane waves including viscous dissipation can be generalized by taking into account both stratification and rotation. We consider an incompressible continuously stratified Boussinesq fluid with constant buoyancy frequency N, rotating around the vertical axis parallel to gravity at a constant angular rotation Ω (i.e. the Coriolis parameter is $f = 2\Omega$). We assume no variation in the transverse (y) direction, which is verified by experimental observation. The velocity is written as ($v_x = \partial_z\psi$, v_y, $v_z = -\partial_x\psi$), v_y being the velocity in the transverse direction and ψ the streamfunction of the in-plane flow. After some calculations of weak nonlinearities, fully detailed in appendix A, one can obtain the evolution equations for the amplitudes of waves 0, 1 and 2:

$$\dot{\Psi}_0 = I_0\Psi_1\Psi_2 - \frac{1}{2}\nu\kappa_0^2\left(1 + \frac{f^2m_0^2}{\kappa_0^2\omega_0^2}\right)\Psi_0, \tag{3.1}$$

$$\dot{\Psi}_1 = I_1\Psi_0\Psi_2^* - \frac{1}{2}\nu\kappa_1^2\left(1 + \frac{f^2m_1^2}{\kappa_1^2\omega_1^2}\right)\Psi_1, \tag{3.2}$$

$$\dot{\Psi}_2 = I_2\Psi_0\Psi_1^* - \frac{1}{2}\nu\kappa_2^2\left(1 + \frac{f^2m_2^2}{\kappa_2^2\omega_2^2}\right)\Psi_2, \tag{3.3}$$

where I_r is

$$I_r = \gamma_r\frac{\ell_p m_q - m_p\ell_q}{2\omega_r\kappa_r^2}\left[\omega_r(\kappa_p^2 - \kappa_q^2) + \ell_r N^2\left(\frac{\ell_p}{\omega_p} - \frac{\ell_q}{\omega_q}\right) + m_r f^2\left(\frac{m_p}{\omega_p} - \frac{m_q}{\omega_q}\right)\right], \tag{3.4}$$

with $\gamma_0 = 1$, $\gamma_{1,2} = -1$, $(p, q, r) = (0, 1, 2)$, or any circular permutation thereof. Here, I_r is an interaction coefficient between the primary and the two secondary waves resulting from the nonlinear term in the Navier–Stokes and incompressibility equations. In the dispersion relation (2.2) and in the interaction coefficient (3.4), the products fm and $N\ell$ appear, highlighting the symmetric role played by stratification for the horizontal wavevector component and by rotation for the vertical wavevector component.

In § 2, we observed that rotation has an influence on the development of the instability. To understand this effect, the growth rate σ of the instability can be extracted using (3.2) and (3.3) assuming a constant amplitude for the primary wave, because we consider only the early times of the instability growth. This amplitude will be defined using the Reynolds number $Re = 2\pi\Psi_0/\nu$. The details of the calculation of

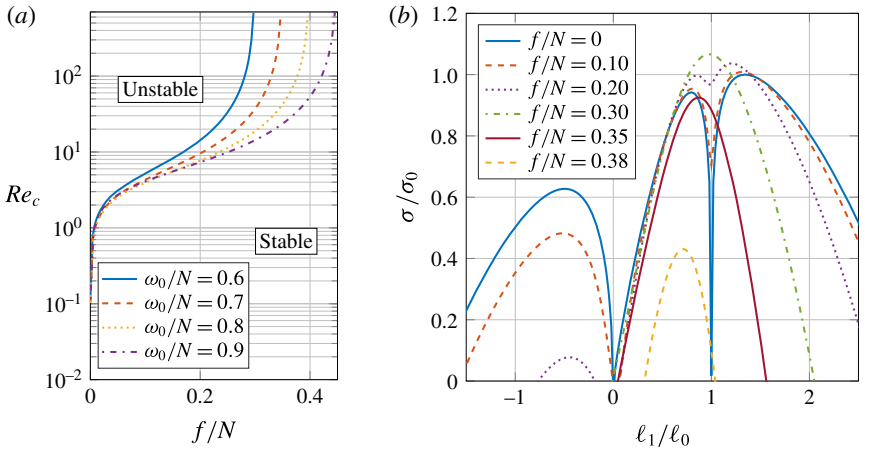

FIGURE 5. (Colour online) (*a*) The evolution of the theoretical threshold of TRI in the case of an infinite plane inertia–gravity wave of horizontal wavenumber $\ell_0 = 80$ m^{-1}. The threshold is represented by the critical Reynolds number $Re_c = 2\pi\Psi_{0,c}/\nu$ and is plotted versus f/N at constant ω_0/N. (*b*) The growth rate (3.6) at different values of the Coriolis parameter f/N, renormalized by the maximum growth rate at $f/N = 0$ ($\sigma_0 = 0.11$ s^{-1}) versus the horizontal component ℓ_1 of one of the secondary wavevectors, for a primary wave at ($\ell_0 = 80$ m^{-1}, $\omega_0/N = 0.8$, $Re = 188$).

the generalized growth rate, which takes into account both rotation and stratification, is in appendix A, yielding

$$\sigma = -\frac{1}{4}\nu\left(\kappa_1^2+\kappa_2^2+\frac{f^2m_1^2}{\omega_1^2}+\frac{f^2m_2^2}{\omega_2^2}\right)+\sqrt{\frac{1}{16}\nu^2\left(\kappa_1^2-\kappa_2^2+\frac{f^2m_1^2}{\omega_1^2}-\frac{f^2m_2^2}{\omega_2^2}\right)^2+I_1I_2|\Psi_0|^2}, \tag{3.5}$$

$$= -\frac{1}{4}\nu\left(\kappa_1^2+\kappa_2^2+\frac{f^2m_1^2}{\omega_1^2}+\frac{f^2m_2^2}{\omega_2^2}\right)+\sqrt{I_1I_2}|\Psi_0|+o(\nu\kappa_{1,2}^2). \tag{3.6}$$

The condition for instability is that the growth rate σ from (3.6) is positive for at least one combination of $\ell_1, m_1, \omega_1, \ell_2, m_2, \omega_1, \omega_2$ that respects the dispersion relation and the resonance conditions. The theoretical threshold in amplitude is defined as the value $\Psi_{0,c}$ of the amplitude when the maximum value of σ is zero. The threshold of TRI depends on the amplitude of the primary wave and on its frequency, but not on its wavelength: if $\boldsymbol{k}_0$, $\boldsymbol{k}_1$ and $\boldsymbol{k}_2$ are multiplied by the same coefficient K, the growth rate (3.6) is multiplied by K^2, and the threshold is unchanged. In figure 5(*a*), we show the amplitude threshold ($Re_c = 2\pi\Psi_{0,c}/\nu$) as a function of f/N for various values of ω_0/N. As underlined by Bourget *et al.* (2014), if $f = 0$ there is no TRI threshold. When rotation is introduced in the system, however, it induces a finite threshold for TRI. This reflects the fact that, as the amplitude of the primary wave vanishes, the frequencies of the secondary waves tend towards zero and ω_0. When there is rotation in the system, a zero-frequency subharmonic wave is no longer allowed, hence the appearance of a threshold in amplitude, which increases with f/N. This threshold tends to infinity as f reaches $\omega_0/2$. A simple explanation for this observation is that for both $\omega_{1,2} > f$ and the temporal resonance condition to be fulfilled, f must be smaller than $\omega_0/2$.

Figure 5(*b*) shows the associated growth rate (3.6) as a function of ℓ_1/ℓ_0 for various values of f/N. For each curve, the growth rate reaches a maximum resulting in a selection criterion for TRI. It should be noted that outside the range of ℓ_1/ℓ_0 presented in the figure, the growth rate tends monotonically towards negative values. In this model, for low values of f/N, rotation has little impact on the maximum growth rate. For larger values of f/N, the maximum growth rate decreases strongly as f increases. This is a general feature, related to the threshold divergence as f approaches $\omega_0/2$.

Within this theoretical framework, one can compute the two wavevectors $\boldsymbol{k}_{\sigma_{max}}$ corresponding to the maximum growth rate of TRI for experiment (*c*) in figure 3. Their tips are represented by grey circles in figure 4. The measured wavevectors fall on this theoretical prediction, within their experimental errors.

3.2. *Finite size effect*

In the case of infinite plane waves, we showed in the previous section that the amplitude instability threshold increases continuously with the Coriolis parameter f/N. From an oceanic perspective, this would mean that inertia–gravity waves at the Equator would be more prone to TRI than waves at higher latitude (because of the latitude dependence of the Coriolis parameter $f = 2\Omega_{Earth} \sin\eta$, where η is the latitude). This does not correspond to existing oceanic observations: numerical simulations (MacKinnon 2005; MacKinnon *et al.* 2013*b*) and field studies (MacKinnon *et al.* 2013*a*) highlight the existence of a critical latitude at $f = \omega_0/2$ where TRI is strongly enhanced. The experiments presented in § 2 show that TRI appears only when rotation is strong enough (compare figures 3*a* and *b*) with other parameters kept constant. The predictions presented in the previous section cannot explain this behaviour and actually seem to show that rotation prevents TRI. The major difference from the experiment lies in the infinite beam width of the plane wave in our theoretical development. The effect of finite size for pure internal waves ($f = 0$) was studied theoretically by Karimi & Akylas (2014). Laboratory experiments have also been performed by Bourget *et al.* (2014), who derived a simple model taking into account the finite size effect of the beam width. The theory by Karimi & Akylas (2014) and the model by Bourget *et al.* (2014) are based on the same premises: the triadic interaction has to be strong enough in the limited time that subharmonic perturbations overlap with the beam. As schematically shown in figure 6(*a*), the secondary waves leave the interaction region of width W with a velocity equal to the projection of their group velocity onto the direction $\boldsymbol{n}_\perp = \boldsymbol{k}_0/\kappa_0$, perpendicular to the primary wave propagation direction. The amplitude of this exit velocity is then $|\boldsymbol{v}_{g,i} \cdot \boldsymbol{n}_\perp|$.

Following the approach of Bourget *et al.* (2014), the time evolution of the secondary wave amplitude also depends on the rate at which these waves leave the interaction region, which we call the advection rate. This rate can be expressed as the ratio of the exit velocity defined above over the width of the primary wave beam. The amplitude equations (3.2) and (3.3) of the secondary waves thus become

$$\dot{\Psi}_1 = I_1 \Psi_0 \Psi_2^* - \frac{1}{2}\left[\nu\kappa_1^2\left(1 + \frac{f^2 m_1^2}{\kappa_1^2 \omega_1^2}\right) + \frac{|\boldsymbol{v}_{g,1} \cdot \boldsymbol{n}_\perp|}{W}\right]\Psi_1, \tag{3.7}$$

$$\dot{\Psi}_2 = I_2 \Psi_0 \Psi_1^* - \frac{1}{2}\left[\nu\kappa_2^2\left(1 + \frac{f^2 m_2^2}{\kappa_2^2 \omega_2^2}\right) + \frac{|\boldsymbol{v}_{g,2} \cdot \boldsymbol{n}_\perp|}{W}\right]\Psi_2. \tag{3.8}$$

Increasing the rotation f affects the time spent by the secondary wave in the primary wave beam in two different ways. First, as f increases, the group velocity is reduced, vanishing at $f = \omega$. Second, changing the rotation affects the direction of propagation.

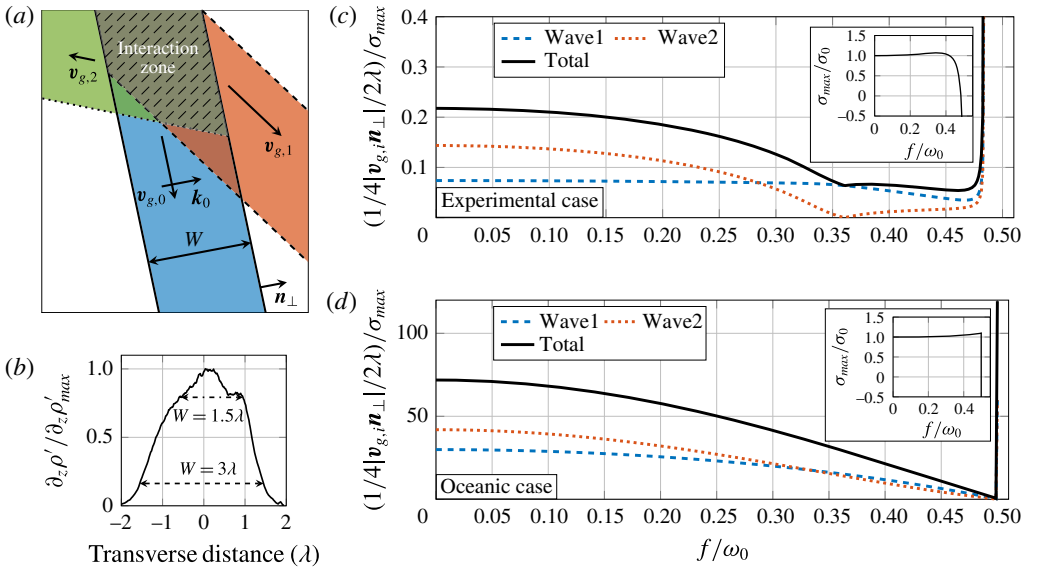

FIGURE 6. (Colour online) (*a*) Schematics of the triadic resonant interaction, highlighting the existence of an interaction zone of width W corresponding to the width of the primary wave. (*b*) Typical transverse profile of the wave amplitude, for the wave presented in figure 3(*a*) extracted by Hilbert transform. (*c*,*d*) The ratio of the outgoing advection rate of the secondary waves away from the primary wave beam over the maximum growth rate of the instability, as a function of f/ω_0. This ratio is shown individually for each secondary wave and also for the sum of both advection rates, which directly compares the two terms of (3.10):$(1/4)(|\boldsymbol{v}_{g,1}\cdot\boldsymbol{n}_\perp|+|\boldsymbol{v}_{g,2}\cdot\boldsymbol{n}_\perp|)/2\lambda\sigma_{max}$. Inset: corresponding maximum growth rate σ_{max} (normalized by the maximum growth rate at $f=0$, σ_0). Two different sets of parameters are considered: (*c*) experimental parameters ($\omega_0/N=0.8$, $\ell_0=80$ m^{-1} and $Re=188$); (*d*) oceanic case, where parameter values are taken from Gayen & Sarkar (2013) and Sun & Pinkel (2013) ($\omega_0/N=0.1$, $\ell_0=6.3\times10^{-2}$ m^{-1} and $Re=3.9\times10^5$).

If the primary and the secondary waves were collinear, the secondary waves would never leave the primary beam. In contrast, when the group velocity of the secondary waves $\boldsymbol{v}_{\boldsymbol{g},(\mathbf{1},\mathbf{2})}$ is not perpendicular to the primary wavevector $\boldsymbol{k}_0$, the secondary waves will leave the primary beam. From (3.7) and (3.8), one can then extract a modified instability growth rate, in the same way as the growth rate (3.6) was extracted in the infinite beam case:

$$\Sigma = -\frac{1}{4}\left(\nu\left(\kappa_1^2+\kappa_2^2+\frac{f^2m_1^2}{\omega_1^2}+\frac{f^2m_2^2}{\omega_2^2}\right)+\frac{|\boldsymbol{v}_{g,1}\cdot\boldsymbol{n}_\perp|}{W}+\frac{|\boldsymbol{v}_{g,2}\cdot\boldsymbol{n}_\perp|}{W}\right) + \sqrt{\frac{1}{16}\left(\nu\left(\kappa_1^2-\kappa_2^2+\frac{f^2m_1^2}{\omega_1^2}-\frac{f^2m_2^2}{\omega_2^2}\right)+\frac{|\boldsymbol{v}_{g,1}\cdot\boldsymbol{n}_\perp|}{W}-\frac{|\boldsymbol{v}_{g,2}\cdot\boldsymbol{n}_\perp|}{W}\right)^2+I_1I_2|\Psi_0|^2}. \tag{3.9}$$

Taking into account the experimental values, $I_1I_2|\Psi_0|^2$ is the leading term inside the square root in this equation, so that

$$\Sigma=\sigma-\frac{1}{4W}(|\boldsymbol{v}_{g,1}\cdot\boldsymbol{n}_\perp|+|\boldsymbol{v}_{g,2}\cdot\boldsymbol{n}_\perp|)+o(\nu\kappa_{1,2}^2)+o\left(\frac{|\boldsymbol{v}_{g,1,2}\cdot\boldsymbol{n}_\perp|}{W}\right). \tag{3.10}$$

A beam will be considered wide when its width W is large compared with the wavelength. In such a case, one recovers expression (3.6) from (3.10). To get an idea of the actual width of our experimental beam, generated as described in § 2.1, figure 6(*b*) shows a typical transverse profile of the beam (measured perpendicular to the direction of propagation of the wave). The effective width of the beam lies between 1.5λ and 3λ.

The relative importance of the advection rate of each secondary wave, $1/4W|\boldsymbol{v}_{g,i}\cdot\boldsymbol{n}_{\perp}|$, versus the growth rate is shown in figure 6(*c*,*d*), where the ratio between the two is plotted as a function of f/ω_0, for two given sets of parameters. Based on figure 6(*b*), the typical beam width was chosen to be $W=2\lambda$. Small values of this ratio correspond to cases where finite size is not a limiting process for TRI, since the secondary waves stay long enough in the primary beam. Figure 6(*c*) corresponds to values used in our experiments. First, we notice that although the advection term is not dominant, which justifies the first-order approximation leading to (3.10), it is not negligible. In addition, we observe the existence of a particular range of f/ω_0 where TRI is more likely to occur. In the range $0<f/\omega_0<0.45$, σ_{max} is fairly constant (see the inset of figure 6*c*), but, in the range $0.35<f/\omega_0<0.45$, the interaction time is larger (low advection rate), which enhances the instability. Figure 6(*d*) shows the same ratio for typical oceanic inertia–gravity waves (characteristics extracted from Gayen & Sarkar (2013) and Sun & Pinkel (2013)). In this case, the advection rate is the dominant term and the range of f/ω_0 favouring TRI is roughly reduced to a single value, close to 0.5. In the ocean, wave beams can be extremely narrow (Lien & Gregg 2001; Gostiaux & Dauxois 2007). In such cases, we can make the assumption that the finite size effect is paramount and that TRI will only appear in the most favourable case, i.e. $f\simeq\omega_0/2$ from figure 6(*d*). This result is consistent with MacKinnon *et al.* (2013*a*,*b*), and gives a sensible explanation for the predominance of TRI at a critical latitude rather than at the Equator.

The approach presented in this section shows that TRI is favoured for a given range of Coriolis parameters. Let us now return to laboratory experiments and check whether this feature can be observed.

4. Experimental instability threshold and secondary wave characteristics

4.1. *Experimental threshold*

We now focus on estimating the threshold of the triadic instability experimentally. To do so, we generate inertia–gravity waves with a given horizontal wavelength ($\ell_0=80\ \mathrm{m}^{-1}$) for a given generator displacement amplitude of 5 mm but with varying frequency ω_0 and Coriolis parameter f. The parameter space is not reduced by keeping a constant amplitude. Indeed, in our experiments Re decreases as ω_0/N decreases. A good approximation is to assume that the Reynolds number is simply proportional to $(\omega_0/N)^2$, in agreement with the experimental measurements. Because ℓ_0 is fixed by the generator, in this configuration, the wave can be described with only two parameters $(\omega_0/N,\ f/N)$. For this reason, the threshold that will be discussed here is a threshold in frequency rather than a threshold in amplitude. In figure 7, we show the numerous experimental measurements in this parameter space. Stable or unstable cases, with respect to TRI, are indicated by a different symbol. For example, for $f/N=0$ the primary wave is stable at $\omega_0/N=0.66$, but is unstable at $\omega_0/N=0.71$, in agreement with previous studies (Bourget *et al.* 2014). These measurements allow one to locate the instability frequency threshold, which lies between the highest frequency for which no TRI is detected and the lowest frequency for which TRI is observed.

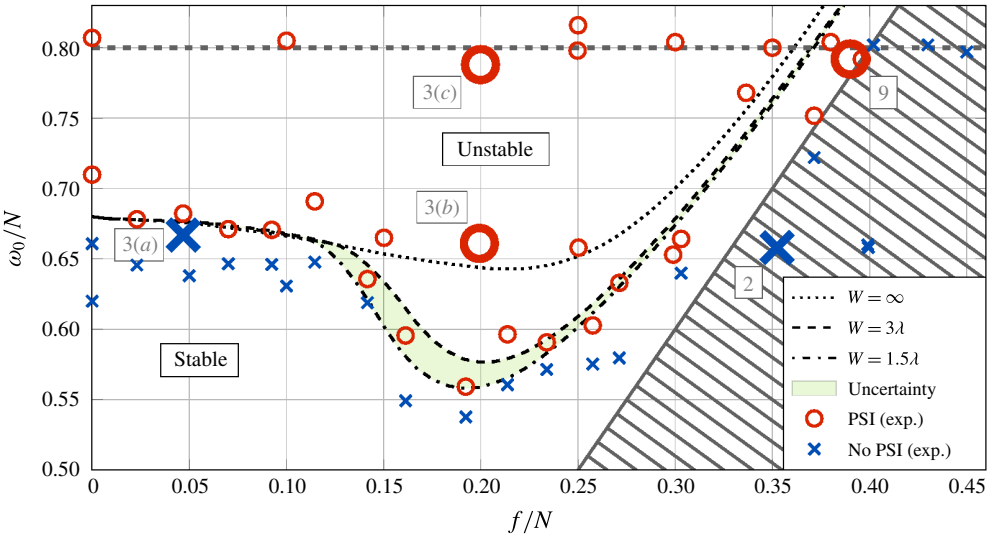

FIGURE 7. (Colour online) Experimental observations showing the triadic resonance stability or instability of a primary wave of dimensionless frequency ω_0/N at Coriolis parameter f/N. The fixed parameters are $\ell_0 = 80$ m^{-1}, $e_0 = 5$ mm, leading to $Re > 100$ for each experiment. The predicted threshold is shown by a dotted line in the infinite beam case, by a dashed line in the finite beam case with a 3-wavelength-wide beam and by a dash-dotted line in the finite beam case with a 1.5-wavelength-wide beam. Our prediction uncertainty due to the uncertainty in the width of the beam is displayed as a light green zone. The hatched zone corresponds to a forbidden zone for TRI: if ω_1 and ω_2 are larger than f, then according to the space resonance condition, ω_0 is larger than $2f$. The larger symbols help to locate on this graph the experiments described in other figures of this article, with the figure number indicated. The horizontal dashed line indicates $\omega_0/N = 0.8$, which corresponds to the experiments presented in figure 8.

For low values of the Coriolis parameter ($f/N < 0.12$), the threshold remains fairly constant. It then decreases to reach a minimal value around $f/N = 0.2$. At larger values of the Coriolis parameter, the threshold follows a limit defined by the line $\omega_0 = 2f$. Below this line (hatched zone in the figure), TRI is forbidden. Indeed, the two secondary frequencies have to be larger than f, so that $\omega_0 = \omega_1 + \omega_2$ has to be larger than $2f$ for the temporal resonance condition to be satisfied.

In the previous section, we wrote a simplified expression Σ for the growth rate of the instability, which takes into account the finite size effect. This growth rate can be used to estimate the threshold of the instability from the model and compare it with experimental observations.

An experimental criterion is needed to determine whether or not the frequency is above the threshold. To find this criterion, we consider the case $f/N = 0$. From figure 7, we estimate that the threshold in this case is located around $\omega_0/N = 0.68$. For these values of f and ω_0, we then calculate the maximum value of $\Sigma(\ell_1)$ (with respect to ℓ_1), later referred to as Σ^0. In what follows, we assume for a given primary wave in the parameter space (ω_0/N, f/N) that any corresponding value of the growth rate Σ that is larger than Σ^0 leads to an unstable case, whereas any value below gives a stable primary wave. To estimate the evolution of the threshold with increasing f/N, we operate as follows.

(i) We choose a given f/N value.
(ii) At $\omega_0/N = 0.8$ (a region always unstable experimentally, whatever the value of f, except in the hatched zone), the maximum value of $\Sigma(\ell_1)$, later referred to as Σ^{max}, is calculated.
(iii) If $\Sigma^{max} > \Sigma^0$, ω_0/N is decreased by a chosen step (in our study this step is $\Delta(\omega_0/N) = 0.02$).
(iv) For the new value of frequency and corresponding amplitude, the new Σ^{max} is calculated.
(v) The procedure is repeated until $\Sigma^{max} < \Sigma^0$. The threshold is therefore determined within a given error (in our study a 2 % error on ω_0/N).

As discussed earlier, because the exact width W of the beam is not known, an additional error is introduced. For this reason, we show in figure 7 the threshold curve in the two cases $W = 1.5\lambda$ and $W = 3\lambda$, which are the limiting values for W according to figure 6(*b*). The band between these two threshold curves represents the margin of error in our estimation of the threshold. We note that this band lies roughly in the region that separates experimental points where TRI takes place from experimental points where the primary wave is stable. The corresponding curve for infinitely wide beams is also shown to emphasize the importance of the finite size effect.

4.2. *Frequencies of the secondary waves*

In figure 7, the good agreement between the model and the experimental threshold prevails until $f/N \approx 0.3$. Above this value, unstable events are observed below the threshold predicted by the model. To get more insight into this feature, we focus on a particular value of the frequency of the primary wave, $\omega_0/N = 0.8$, for different values of f/N. For each run, a temporal fast Fourier transform of the vertical density gradient $\partial_z \rho'$ is performed on the signal recorded during the steady state ($t = 90T_0$) using a $30T_0$ time window. In figure 8, showing the corresponding spectrum, there is a strong peak at $\omega_0/N = 0.8$, corresponding to the forcing frequency, and a pair of twin peaks, as expected, for $0 < f/N < 0.4$, corresponding to secondary waves of frequencies ω_1 and ω_2, smaller than ω_0. Above 0.4, the primary wave is stable, as expected. For every value of f/N, there is a symmetry with respect to the position $\omega_0/2N$, and the temporal resonance condition is fulfilled: $\omega_1 + \omega_2 = \omega_0$. As expected from the dispersion relation, as f/N increases the main secondary peaks move closer to $\omega_0/2N$, bringing TRI closer to what is commonly known as PSI. Interestingly, rotation not only has an influence on secondary wave characteristics but may also foster the instability. In this context, the experiment at $f/N = 0.25$ is particularly interesting. One can see that the instability is stronger, with several secondary frequencies, which are much weaker in the cases $f/N = 0.2$ and $f/N = 0.3$ and do not appear in the other cases. This enhanced instability can be explained by considering the secondary wave 1. Its frequency ($\omega_1/N \simeq 0.51$) is close to $2f$. We demonstrated in the theoretical analysis of the finite size effect that a wave at this frequency, now considered as the primary wave, is most likely to undergo a secondary instability, thereby creating the observed multiple TRI.

Let us now turn to the particular case $0.35 < f/N < 0.4$. We observe in figure 8 that one of the secondary waves (later referred to as 1) has a frequency above f and the other one (later referred to as 2) has a frequency below f. In this case, the secondary wave 2 is a sub-inertial wave, and its existence is not taken into account in our theoretical approach, where we assumed, for $i = (0, 1, 2)$, that $f < \omega_i < N$. This observation may be related to the discrepancy seen in figure 7 for $f > 0.3$.

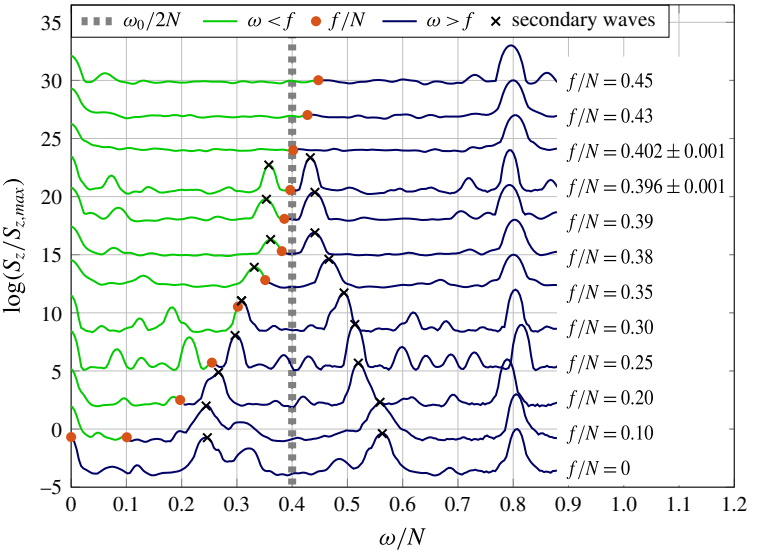

FIGURE 8. (Colour online) Renormalized amplitude of the fast Fourier transform of the vertical gradient of density over a $30T_0$ time window at $t \approx 90T_0$, for a primary wave propagating at $\omega_0/N \simeq 0.8$ and for various values of f/N, which correspond to $63.2° < \theta < 68.9°$. For the sake of clarity, the spectra are shifted vertically by a multiple of 3, the vertical axis values corresponding to the case $f/N = 0$. On each spectrum, a red dot indicates the value of f/N and separates it into two parts, one in green on the left where $\omega < f$ and one on the right where $\omega > f$. A vertical dashed line indicates $\omega/N = 0.4$, which corresponds roughly to $\omega_0/N/2$. On each spectrum, the peak on the right represents the primary wave, and daughter waves correspond to the other peaks, identified with a cross. For the sake of clarity, the value f/N is displayed with full precision only when it is necessary, for the experiments just above and just below the threshold.

Snapshots of an experimental vertical density-gradient field at different times are presented in figure 9 for the particular case $f/N = 0.39$. At early time, a plane wave propagates from the top left corner to the bottom right corner of the field of view (figure 9*a*). A few oscillating periods later, perturbations of the wave field appear below the wave maker (figure 9*b*). These perturbations continue to evolve until a stationary state is reached (figure 9*c*). This behaviour is similar (even at long times) to what was observed when ω_1 and ω_2 were larger than f (for example, figure 3*c*). The experimental time series at a point 5 cm below the wavemaker filtered at ω_0, ω_1 and ω_2 respectively are shown in figure 9(*d–f*), confirming that a stationary regime is reached for the configuration under consideration.

From a theoretical point of view, the existence of sub-inertial waves in the case of TRI was predicted for ω_0 slightly smaller than $2f$ by Young *et al.* (2008). A comparison between this theory and the experiments is not possible because the viscosity and finite size effect of the primary wave are of paramount importance in the laboratory case. A possible explanation for this type of sub-inertial waves could be a misalignment between the background density gradient and the axis of rotation. As mentioned in § 2.1, however, this alignment was carefully controlled in the building of the rotating platform, leading to a maximum angle of 0.1°, too small to explain the observed phenomenon. A formal theory that incorporated our experimental configuration would be interesting for the understanding of this phenomenon for which the interpretation currently remains open.

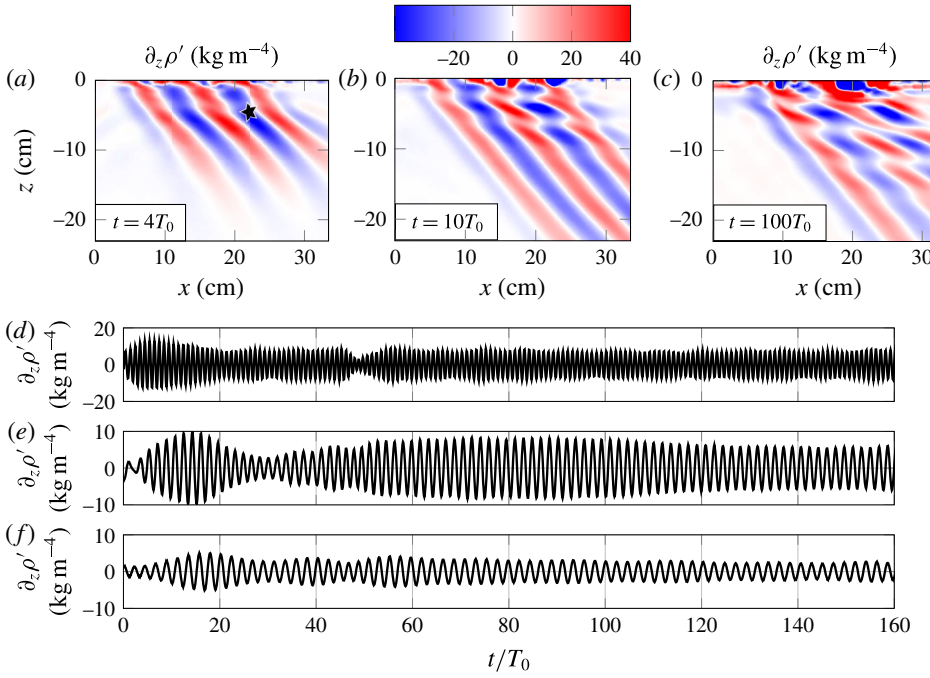

FIGURE 9. (Colour online) (*a*,*b*,*c*) Snapshots of the vertical density-gradient field for (*a*) $t = 4T_0$, (*b*) $t = 10T_0$ and (*c*) $t = 100T_0$, with T_0 the primary wave period. The wave is propagating from the top left to the bottom right. The Coriolis parameter is $f/N = 0.39$, the wave frequency is $\omega_0/N = 0.8$ and the motion amplitude of the generator is 0.5 cm. (*d*,*e*,*f*) Vertical density gradient as a function of time for a point located 5 cm below the wavemaker (indicated by a star in *a*), filtered at ω_0 (*d*), ω_1 (*e*) and ω_2 (*f*).

5. Conclusions

In an experimental approach, we have studied the influence of ambient rotation on TRI. Using the same experimental device as in Bourget *et al.* (2013) placed on a rotating platform, we generated controlled inertia–gravity waves and characterized them through their dispersion relation. In this set-up, resonance conditions for TRI were verified. Using the analytical development of Bourget *et al.* (2013), we introduced the effect of rotation, allowing us to study how growth rates are modified. The experimental secondary wave frequencies and wavevectors are in good agreement with the theoretical maximum growth rate.

This approach, however, only works for infinite plane waves and cannot explain the experimental evolution of the threshold with rotation rate. For finite size beams, one has to take into account the possibility that secondary waves leave the interaction region, resulting in a decreased growth rate. Following Bourget *et al.* (2014), we modelled this finite size effect by an advection rate. Using this model, we were able to predict the evolution of the instability threshold with rotation and show that TRI is enhanced at a finite non-zero value of the Coriolis parameter. This characteristic value depends strongly on the size of the primary wave beam. In the ocean, viscosity plays a much lesser role than in experiments, due to a larger Reynolds number. For this reason, comparisons of our results with oceanic situations are always delicate. Nevertheless, in the case of the enhanced instability that we observe in a range of the

Coriolis parameter, a projection of the experimental results and theoretical explanation for small viscosity and small width of the wave beam provides a sensible explanation to the critical latitude phenomenon observed *in situ* and in numerical simulation by MacKinnon (2005) and MacKinnon *et al.* (2013*a*,*b*). In addition, for some rotation rates, the temporal spectrum observed in our experiment exhibits multiple peaks, i.e. multiple triads. This feature might open interesting perspectives regarding mixing in the ocean dynamics as well as in the understanding of the spectral content of the internal wave background in the ocean (Garrett & Munk 1972).

At larger rotation rates, a discrepancy between observations and our model is observed. This discrepancy may be related to the presence of one sub-inertial secondary wave that is neither transient nor evanescent. This type of wave is not taken into account in the model. Such waves were theoretically and numerically predicted for an inviscid case (Young *et al.* 2008). The observation of these waves remains puzzling, however, and it would be interesting to study them theoretically. Several questions can be raised. In the same way that selection criteria were established for the classical TRI secondary waves, can analogous criteria be obtained when a secondary wave is sub-inertial? How is the direction of propagation of these sub-inertial waves chosen? How is the appearance of these waves related to the primary wave remaining stable as soon as $2f > \omega_0$ (hatched region for TRI in figure 7)?

Acknowledgements

This work has been partially supported by the ONLITUR grant ANR-2011-BS04-006-01 and achieved thanks to the resources of PSMN from ENS de Lyon. We thank T. Dauxois and A. Venaille for helpful discussions and R. Ecke for careful proofreading.

Appendix A. The TRI theory for an inertia–gravity wave in the presence of viscosity

A.1. *Viscous plane wave*

The two-dimensional dynamics (in the x, z coordinates) of a Boussinesq fluid is usually described by the following three equations:

$$\frac{\partial b}{\partial t} + J(b, \psi) = N^2 \frac{\partial \psi}{\partial x}, \tag{A 1}$$

$$\frac{\partial v_y}{\partial t} + J(v_y, \psi) + f\frac{\partial \psi}{\partial z} = \nu \Delta v_y, \tag{A 2}$$

$$\frac{\partial \nabla^2 \psi}{\partial t} + J(\nabla^2 \psi, \psi) - f\frac{\partial v_y}{\partial z} = -\frac{\partial b}{\partial x} + \nu \Delta^2 \psi, \tag{A 3}$$

where $b = -g\rho'/\bar{\rho}$ is the buoyancy perturbation, with $\bar{\rho}$ and ρ' being respectively the mean density and the difference between the density and the mean density, such that $\rho = \bar{\rho} + \rho'$. Here, J is the Jacobian operator, defined as $J(f_1, f_2) = \partial_x f_1 \partial_z f_2 - \partial_z f_1 \partial_x f_2$, and ψ is a function that can be interpreted as the current function in the case of purely internal waves (as $f = 0$ imposes $\boldsymbol{v} \cdot \boldsymbol{e_y} = v_y = 0$). We assume that all quantities are invariant in the transverse y direction. This assumption is supported by experimental observations that are detailed in § 2. Therefore, the incompressible flow condition permits the velocity to be written as $\boldsymbol{v} = (\partial_z \psi, v_y, -\partial_x \psi)$. Because we are

interested in triadic interactions, we look for solutions of the form

$$b = \sum_{j=0}^{2} R_j(t) \exp(\mathrm{i}(\boldsymbol{k_j} \cdot \boldsymbol{r} - \omega_j t)) + \text{c.c.}, \tag{A 4}$$

$$v_y = \sum_{j=0}^{2} V_j(t) \exp(\mathrm{i}(\boldsymbol{k_j} \cdot \boldsymbol{r} - \omega_j t)) + \text{c.c.}, \tag{A 5}$$

$$\psi = \sum_{j=0}^{2} \Psi_j(t) \exp(\mathrm{i}(\boldsymbol{k_j} \cdot \boldsymbol{r} - \omega_j t)) + \text{c.c.}, \tag{A 6}$$

where $\boldsymbol{k}_j = (l, 0, m)$ has no transverse component. Substituting these solutions into (A 1), (A 2) and (A 3), one obtains

$$\sum_{j=0}^{2} [\dot{R}_j - \mathrm{i}\omega_j R_j - \mathrm{i}N^2 \ell_j \Psi_j] \exp(\mathrm{i}(\boldsymbol{k_j} \cdot \boldsymbol{r} - \omega_j t)) + \text{c.c.} = -J(b, \psi), \tag{A 7}$$

$$\sum_{j=0}^{2} [\dot{V}_j - \mathrm{i}\omega_j V_j + \nu\kappa_j^2 V_j + \mathrm{i}f m_j \Psi_j] \exp(\mathrm{i}(\boldsymbol{k_j} \cdot \boldsymbol{r} - \omega_j t)) + \text{c.c.} = -J(v_y, \psi), \tag{A 8}$$

$$\sum_{j=0}^{2} [-\kappa_j^2(\dot{\Psi}_j - \mathrm{i}\omega_j \Psi_j) + \mathrm{i}\ell_j R_j - \nu\kappa_j^4 \Psi_j - \mathrm{i}f m_j V_j] \exp(\mathrm{i}(\boldsymbol{k_j} \cdot \boldsymbol{r} - \omega_j t)) + \text{c.c.} = -J(\nabla^2\psi, \psi), \tag{A 9}$$

where for any variable A, $\dot{A}$ stands for the temporal derivative of A.

A.1.1. *Resonance conditions*

The Jacobians in (A 7)–(A 9) can be written as

$$\begin{aligned} J(b, \psi) \;=\; & \sum_{p=0}^{2} \sum_{q \neq p} [(-\ell_p m_q + m_p \ell_q) R_p \Psi_q] \exp(\mathrm{i}((\boldsymbol{k_p} + \boldsymbol{k_q}) \cdot \boldsymbol{r} - (\omega_p + \omega_q)t)) \\ & - [(-l_p m_q + m_p \ell_q) R_p \Psi_q^*] \exp(\mathrm{i}((\boldsymbol{k_p} - \boldsymbol{k_q}) \cdot \boldsymbol{r} - (\omega_p - \omega_q)t)) + \text{c.c.}, \end{aligned} \tag{A 10}$$

$$\begin{aligned} J(v_y, \psi) \;=\; & \sum_{p=0}^{2} \sum_{q \neq p} [(-\ell_p m_q + m_p \ell_q) V_p \Psi_q] \exp(\mathrm{i}((\boldsymbol{k_p} + \boldsymbol{k_q}) \cdot \boldsymbol{r} - (\omega_p + \omega_q)t)) \\ & - [(-\ell_p m_q + m_p \ell_q) V_p \Psi_q^*] \exp(\mathrm{i}((\boldsymbol{k_p} - \boldsymbol{k_q}) \cdot \boldsymbol{r} - (\omega_p - \omega_q)t)) + \text{c.c.}, \end{aligned} \tag{A 11}$$

$$\begin{aligned} J(\nabla^2\psi, \psi) \;=\; & \sum_{p=0}^{2} \sum_{q \neq p} [(\ell_p m_q - m_p \ell_q) \kappa_p^2 \Psi_p \Psi_q] \exp(\mathrm{i}((\boldsymbol{k_p} + \boldsymbol{k_q}) \cdot \boldsymbol{r} - (\omega_p + \omega_q)t)) \\ & - [(\ell_p m_q - m_p \ell_q) \kappa_p^2 \Psi_p \Psi_p^*] \exp(\mathrm{i}((\boldsymbol{k_p} - \boldsymbol{k_q}) \cdot \boldsymbol{r} - (\omega_p - \omega_q)t)) + \text{c.c.} \end{aligned} \tag{A 12}$$

By averaging both the left-hand sides and the right-hand sides of (A 7)–(A 9) over the period of a wave, we obtain the evolution of a particular wave $(\boldsymbol{k}_r, \omega_r)$ associated with the streamfunction Ψ_r, in which $r = 0$, 1 or 2. The resonant terms on the right-hand

side that balance the left-hand side correspond to the waves fulfilling two conditions: a spatial resonance condition

$$\boldsymbol{k}_0 = \boldsymbol{k}_1 + \boldsymbol{k}_2 \tag{A 13}$$

and a temporal resonance condition

$$\omega_0 = \omega_1 + \omega_2. \tag{A 14}$$

In the following, we consider that the frequencies are defined positive and that ω_1 and ω_2 are smaller than ω_0. The difference interactions $\omega_1 - \omega_2 = \pm\omega_0$ are neutrally stable and do not play a role in our study.

A.1.2. *Zeroth-order relations*

The usual inviscid linear dynamics of (A 7) and (A 8) provides the polarization expressions

$$R_j = -\frac{N^2 \ell_j}{\omega_j}\Psi_j, \tag{A 15}$$

$$V_j = \frac{f m_j}{\omega_j}\Psi_j. \tag{A 16}$$

The zeroth-order assumption, $\dot{R}_j \ll \omega_j R_j$ in (A 9) yields the dispersion relation

$$\omega_j^2 = N^2\frac{\ell_j^2}{\kappa_j^2} + f^2\frac{m_j^2}{\kappa_j^2}. \tag{A 17}$$

Keeping only resonant terms and using the polarization equations (A 15) and (A 16), the Jacobians can be written as

$$\begin{aligned} J(b,\psi) \;=\; & (\ell_1 m_2 - m_1\ell_2)N^2\left(\frac{\ell_1}{\omega_1} - \frac{\ell_2}{\omega_2}\right)\Psi_1\Psi_2\exp(\mathrm{i}(\boldsymbol{k_0}\cdot\boldsymbol{r} - \omega_0 t)) \\ & - (\ell_0 m_2 - m_0\ell_2)N^2\left(\frac{\ell_0}{\omega_0} - \frac{\ell_2}{\omega_2}\right)\Psi_0\Psi_2^*\exp(\mathrm{i}(\boldsymbol{k_1}\cdot\boldsymbol{r} - \omega_1 t)) \\ & - (\ell_0 m_1 - m_0\ell_1)N^2\left(\frac{\ell_0}{\omega_0} - \frac{\ell_1}{\omega_1}\right)\Psi_0\Psi_1^*\exp(\mathrm{i}(\boldsymbol{k_2}\cdot\boldsymbol{r} - \omega_2 t)) + \mathrm{NRT}, \end{aligned} \tag{A 18}$$

$$\begin{aligned} J(v,\psi) \;=\; & -(\ell_1 m_2 - m_1\ell_2)f\left(\frac{m_1}{\omega_1} - \frac{m_2}{\omega_2}\right)\Psi_1\Psi_2\exp(\mathrm{i}(\boldsymbol{k_0}\cdot\boldsymbol{r} - \omega_0 t)) \\ & + (\ell_0 m_2 - m_0\ell_2)f\left(\frac{m_0}{\omega_0} - \frac{m_2}{\omega_2}\right)\Psi_0\Psi_2^*\exp(\mathrm{i}(\boldsymbol{k_1}\cdot\boldsymbol{r} - \omega_1 t)) \\ & + (\ell_0 m_1 - m_0\ell_1)f\left(\frac{m_0}{\omega_0} - \frac{m_1}{\omega_1}\right)\Psi_0\Psi_1^*\exp(\mathrm{i}(\boldsymbol{k_2}\cdot\boldsymbol{r} - \omega_2 t)) + \mathrm{NRT}, \end{aligned} \tag{A 19}$$

$$\begin{aligned} J(\nabla^2\psi,\psi) \;=\; & (\ell_1 m_2 - m_1\ell_2)(\kappa_1^2 - \kappa_2^2)\Psi_1\Psi_2\exp(\mathrm{i}(\boldsymbol{k_0}\cdot\boldsymbol{r} - \omega_0 t)) \\ & - (\ell_0 m_2 - m_0\ell_2)(\kappa_0^2 - \kappa_2^2)\Psi_0\Psi_2^*\exp(\mathrm{i}(\boldsymbol{k_1}\cdot\boldsymbol{r} - \omega_1 t)) \\ & - (\ell_0 m_1 - m_0\ell_1)(\kappa_0^2 - \kappa_1^2)\Psi_0\Psi_1^*\exp(\mathrm{i}(\boldsymbol{k_2}\cdot\boldsymbol{r} - \omega_2 t)) + \mathrm{NRT}, \end{aligned} \tag{A 20}$$

where NRT stands for non-resonant terms that are not important in the problem.

A.2. *First-order expansion: slow amplitude variation*

We make the further assumption that the amplitude Ψ_j varies slowly with respect to the period of the wave. It is therefore appropriate to consider that $\dot{\Psi}_j \ll \omega_j \Psi_j$. Use of this assumption in the derivative of (A 15) and (A 16) yields

$$\dot{R}_j = -\frac{N^2 \ell_j}{\omega_j}\dot{\Psi}_j, \tag{A 21}$$

$$\dot{V}_j = \frac{f m_j}{\omega_j}\dot{\Psi}_j. \tag{A 22}$$

Substituting these equations into (A 8), one obtains

$$V_0 = \frac{-\gamma_0 f \beta_0 \Psi_1 \Psi_2 + \mathrm{i} f m_0 \Psi_0 + f\dfrac{m_0}{\omega_0}\dot{\Psi}_0}{\mathrm{i}\omega_0 - \nu\kappa_0^2}, \tag{A 23}$$

$$V_1 = \frac{-\gamma_1 f \beta_1 \Psi_0 \Psi_2^* + \mathrm{i} f m_1 \Psi_1 + f\dfrac{m_1}{\omega_1}\dot{\Psi}_1}{\mathrm{i}\omega_1 - \nu\kappa_1^2}, \tag{A 24}$$

$$V_2 = \frac{-\gamma_2 f \beta_2 \Psi_0 \Psi_1^* + \mathrm{i} f m_2 \Psi_2 + f\dfrac{m_2}{\omega_2}\dot{\Psi}_2}{\mathrm{i}\omega_2 - \nu\kappa_2^2}, \tag{A 25}$$

where $\gamma_0 = 1$, $\gamma_{1,2} = -1$ and

$$\beta_r = (\ell_p m_q - m_p \ell_q)\left(\frac{m_p}{\omega_p} - \frac{m_q}{\omega_q}\right), \tag{A 26}$$

with $(p, q, r) = (0, 1, 2)$ or any circular permutation. One gets for (A 9)

$$R_0 = -\frac{\mathrm{i}}{\ell_0}[\kappa_0^2(\dot{\Psi}_0 - \mathrm{i}\omega_0\Psi_0) + \nu\kappa_0^4\Psi_0 - \gamma_0\alpha_0\Psi_1\Psi_2 + \mathrm{i} f m_0 V_0], \tag{A 27}$$

$$R_1 = -\frac{\mathrm{i}}{\ell_1}[\kappa_1^2(\dot{\Psi}_1 - \mathrm{i}\omega_1\Psi_1) + \nu\kappa_1^4\Psi_1 - \gamma_1\alpha_1\Psi_0\Psi_2^* + \mathrm{i} f m_1 V_1], \tag{A 28}$$

$$R_2 = -\frac{\mathrm{i}}{\ell_2}[\kappa_2^2(\dot{\Psi}_2 - \mathrm{i}\omega_2\Psi_2) + \nu\kappa_2^4\Psi_2 - \gamma_2\alpha_2\Psi_0\Psi_1^* + \mathrm{i} f m_2 V_2], \tag{A 29}$$

where

$$\alpha_r = (\ell_p m_q - m_p \ell_q)(\kappa_p^2 - \kappa_q^2), \tag{A 30}$$

with $(p, q, r) = (0, 1, 2)$ or any circular permutation. Therefore, (A 7) leads to

$$\frac{N^2\ell_0}{\omega_0}\dot{\Psi}_0 + \mathrm{i}\omega_0 R_0 + \mathrm{i}N^2\ell_0\Psi_0 = \gamma_0\delta_0 N^2\Psi_1\Psi_2, \tag{A 31}$$

where

$$\delta_r = (\ell_p m_q - m_p \ell_q)\left(\frac{\ell_p}{\omega_p} - \frac{\ell_q}{\omega_q}\right), \tag{A 32}$$

with $(p, q, r) = (0, 1, 2)$ or any circular permutation. The time derivative of the wave amplitude, $\dot{\Psi}_0$, is related to the other wave amplitudes through

$$\frac{N^2\ell_0^2}{\omega_0^2}\dot{\Psi}_0 + \kappa_0^2(\dot{\Psi}_0 - \mathrm{i}\omega_0\Psi_0) + \nu\kappa_0^4\Psi_0 - \gamma_0\alpha_0\Psi_1\Psi_2 + \mathrm{i}fm_0\left(\frac{-\gamma_0 f\beta_0\Psi_1\Psi_2 + \mathrm{i}fm_0\Psi_0 + f\dfrac{m_0}{\omega_0}\dot{\Psi}_0}{\mathrm{i}\omega_0 - \nu\kappa_0^2}\right) + \mathrm{i}\frac{N^2\ell_0}{\omega_0}\Psi_0 = \gamma_0\frac{\ell_0}{\omega_0}\delta_0 N^2\Psi_1\Psi_2. \quad (A\,33)$$

The zeroth order of the previous equation is simply the dispersion relation and disappears because the considered waves propagate according to this relation. Therefore, we can develop this expression at first order in $\dot{\Psi}_0$, ν and $\Psi_1\Psi_2$, which means that the viscous and nonlinear terms have effects of comparable amplitude in the time evolution of Ψ_0. This first-order development yields

$$\dot{\Psi}_0 = \frac{\gamma_0}{2\kappa_0^2}\left(\alpha_0 + \frac{\delta_0 N^2\ell_0}{\omega_0} + \frac{f^2 m_0\beta_0}{\omega_0}\right)\Psi_1\Psi_2 - \frac{1}{2}\nu\left(\kappa_0^2 + \frac{f^2 m_0^2}{\omega_0^2}\right)\Psi_0. \quad (A\,34)$$

The evolution of Ψ_0 is driven by two terms. The first one is an interaction term between the two other resonant waves. The second one is a viscosity term enhanced by rotation. Rotation turns the two-dimensional back-and-forth movement of the fluid associated with purely gravitational waves into tilted ellipses, which lengthens the fluid particle trajectories during a period, thereby increasing the viscous damping.

Generalization of this procedure to wave 1 and wave 2 yields

$$\dot{\Psi}_0 = I_0\Psi_1\Psi_2 - \frac{1}{2}\nu\kappa_0^2\left(1 + \frac{f^2 m_0^2}{\kappa_0^2\omega_0^2}\right)\Psi_0, \quad (A\,35)$$

$$\dot{\Psi}_1 = I_1\Psi_0\Psi_2^* - \frac{1}{2}\nu\kappa_1^2\left(1 + \frac{f^2 m_1^2}{\kappa_1^2\omega_1^2}\right)\Psi_1, \quad (A\,36)$$

$$\dot{\Psi}_2 = I_2\Psi_0\Psi_1^* - \frac{1}{2}\nu\kappa_2^2\left(1 + \frac{f^2 m_2^2}{\kappa_2^2\omega_2^2}\right)\Psi_2, \quad (A\,37)$$

where I_r is

$$\begin{aligned} I_r &= \frac{\gamma_r}{2\kappa_r^2}\left(\alpha_r + \frac{\delta_r N^2\ell_r}{\omega_r} + \frac{f^2 m_r\beta_r}{\omega_r}\right) \\ &= \gamma_r\frac{\ell_p m_q - m_p\ell_q}{2\omega_r\kappa_r^2}\left[\omega_r(\kappa_p^2 - \kappa_q^2) + \ell_r N^2\left(\frac{\ell_p}{\omega_p} - \frac{\ell_q}{\omega_q}\right) + m_r f^2\left(\frac{m_p}{\omega_p} - \frac{m_q}{\omega_q}\right)\right]. \quad (A\,38) \end{aligned}$$

REFERENCES

BENIELLI, D. & SOMMERIA, J. 1998 Excitation and breaking of internal gravity waves by parametric instability. *J. Fluid Mech.* **374**, 117–144.

BORDES, G., MOISY, F., DAUXOIS, T. & CORTET, P.-P. 2012 Experimental evidence of a triadic resonance of plane intertial waves in a rotating fluid. *Phys. Fluids* **24**, 014105.

BOURGET, B., DAUXOIS, T., JOUBAUD, S. & ODIER, P. 2013 Experimental study of parametric subharmonic instability for internal plane waves. *J. Fluid Mech.* **723**, 1–20.

BOURGET, B., SCOLAN, H., DAUXOIS, T., LEBARS, M., ODIER, P. & JOUBAUD, S. 2014 Finite-size effects in parametric subharmonic instability. *J. Fluid Mech.* **759**, 739–750.

BROUZET, C., SIBGATULLIN, I. N., SCOLAN, H., ERMANYUK, E. V. & DAUXOIS, T. 2016 Internal wave attractors examined using laboratory experiments and 3D simulations. *J. Fluid Mech.* **793**, 109–131.

CLARK, H. A. & SUTHERLAND, B. R. 2010 Generation, propagation, and breaking of an internal wave beam. *Phys. Fluids* **22** (7), 076601.

DALZIEL, S. B., HUGHES, G. O. & SUTHERLAND, B. R. 2000 Whole-field density measurements by synthetic schlieren. *Exp. Fluids* **28**, 322–335.

FINCHAM, A. & DELERCE, G. 2000 Advanced optimization of correlation imaging velocimetry algorithms. *Exp. Fluids (Suppl.)* S13–S22.

FLANDRIN, P. 1999 *Time-Frequency/Time-Scale Analysis, Time-Frequency Toolbox for Matlab©*. Academic.

FORTUIN, J. M. H. 1960 Theory and application of two supplementary methods of constructing density gradient columns. *J. Polym. Sci.* **44** (144), 505–515.

GARRETT, C. J. R. & MUNK, W. H. 1972 Space-time scales of internal waves. *Geophys. Fluid Dyn.* **3**, 225–264.

GAYEN, B. & SARKAR, S. 2013 Degradation of an internal wave beam by parametric subharmonic instability in an upper ocean pycnocline. *J. Geophys. Res.* **118** (9), 4689–4698.

GOSTIAUX, L. & DAUXOIS, T. 2007 Laboratory experiments on the generation of internal tidal beams over steep slopes. *Phys. Fluids* **19** (2), 028102.

GOSTIAUX, L., DAUXOIS, T., DIDELLE, H., SOMMERIA, J. & VIBOUD, S. 2006 Quantitative laboratory observations of internal wave reflection on ascending slopes. *Phys. Fluids* **18**, 056602.

HASSELMANN, K. 1967 A criterion for nonlinear wave stability. *J. Fluid Mech.* **30** (04), 737–739.

HAZEWINKEL, J. & WINTERS, K. B. 2011 PSI of the internal tide on a β plane: flux divergence and near-inertial wave propagation. *J. Phys. Oceanogr.* **41** (9), 1673–1682.

HIBIYA, T. 2004 Latitudinal dependence of diapycnal diffusivity in the thermocline estimated using a finescale parameterization. *Geophys. Res. Lett.* **31** (1), L01301.

KARIMI, H. H. & AKYLAS, T. R. 2014 Parametric subharmonic instability of internal waves: locally confined beams versus monochromatic wavetrains. *J. Fluid Mech.* **757**, 381–402.

KOUDELLA, C. R. & STAQUET, C. 2006 Instability mechanisms of a two-dimensional progressive internal gravity wave. *J. Fluid Mech.* **548**, 165–196.

LIEN, R. C. & GREGG, M. C. 2001 Observations of turbulence in a tidal beam and across a coastal ridge. *J. Geophys. Res.* **106** (C3), 4575.

MACKINNON, J. A. 2005 Subtropical catastrophe: significant loss of low-mode tidal energy at 28.9°. *Geophys. Res. Lett.* **32** (15), L15605.

MACKINNON, J. A., ALFORD, M. H., PINKEL, R., KLYMAK, J. & ZHAO, Z. 2013*a* The latitudinal dependence of shear and mixing in the Pacific transiting the critical latitude for PSI. *J. Phys. Oceanogr.* **43** (1), 3–16.

MACKINNON, J. A., ALFORD, M. H., SUN, O., PINKEL, R., ZHAO, Z. & KLYMAK, J. 2013*b* Parametric subharmonic instability of the internal tide at 29 °N. *J. Phys. Oceanogr.* **43** (1), 17–28.

MCCOMAS, C. H. & BRETHERTON, F. P. 1977 Resonant interaction of oceanic internal waves. *J. Geophys. Res.* **82** (9), 1397–1412.

MERCIER, M. J., GARNIER, N. B. & DAUXOIS, T. 2008 Reflection and diffraction of internal waves analyzed with the Hilbert transform. *Phys. Fluids* **20**, 086601.

MERCIER, M. J., MARTINAND, D., MATHUR, M., GOSTIAUX, L., PEACOCK, T. & DAUXOIS, T. 2010 New wave generation. *J. Fluid Mech.* **657**, 308–334.

MÜLLER, P., HOLLOWAY, G., HENYEY, F. & POMPHREY, N. 1986 Nonlinear interactions among internal gravity waves. *Rev. Geophys.* **24** (3), 493.

OSTER, G. & YAMAMOTO, M. 1963 Density gradient techniques. *Chem. Rev.* **63** (3), 257–268.

SIMMONS, H. L. 2008 Spectral modification and geographic redistribution of the semi-diurnal internal tide. *Ocean Model.* **21** (3–4), 126–138.

STAQUET, C. & SOMMERIA, J. 2002 Internal gravity waves: from instabilities to turbulence. *Annu. Rev. Fluid Mech.* **34** (1), 559–593.

SUN, O. M. & PINKEL, R. 2013 Subharmonic energy transfer from the semidiurnal internal tide to near-diurnal motions over Kaena Ridge, Hawaii. *J. Phys. Oceanogr.* **43** (4), 766–789.

SUTHERLAND, B. R. 2010 *Internal Gravity Waves*. Cambridge University Press.

SUTHERLAND, B. R. 2013 The wave instability pathway to turbulence. *J. Fluid Mech.* **724**, 1–4.

SUTHERLAND, B. R., DALZIEL, S. B., HUGHES, G. O. & LINDEN, P. F. 1999 Visualization and measurement of internal waves by 'synthetic schlieren'. Part 1. Vertically oscillating cylinder. *J. Fluid Mech.* **390**, 93–126.

YOUNG, W. R., TSAND, Y. K. & BALMFORTH, N. J. 2008 Near-inertial parametric subharmonic instability. *J. Fluid Mech.* **607**, 25–49.